Lawrence Berkeley National Laboratory
LBL Publications

Title
Wetter California Projected by CMIP6 Models With Observational Constraints Under a High GHG Emission Scenario

Permalink
https://escholarship.org/uc/item/26t1z0c5

Journal
Earth's Future, 10(4)

ISSN
2328-4277

Authors

Li, Fa
Zhu, Qing
Riley, William J
et al.

Publication Date
2022-04-01

DOI
10.1029/2022ef002694

Peer reviewed

Earth's Future

Key Points:

- Coupled Model Intercomparison Project Phase 6 models projected wide ranges of precipitation changes over California, which do not even agree on the sign of changes
- Up to 71% of Earth system model projection uncertainties could be robustly reduced by using observed teleconnection patterns
- California precipitation will increase by 10–34% and 7–32% over northern and southern regions by the end of the 21st century

Author Contributions:
Conceptualization: Qing Zhu
Formal analysis: Qing Zhu
Methodology: Fa Li, Qing Zhu, Kunxiaojia Yuan
Software: Fa Li, Kunxiaojia Yuan
Supervision: Qing Zhu, Huayi Wu, Zhipeng Gui
Validation: William J. Riley, Kunxiaojia Yuan
Writing – original draft: Fa Li

Wetter California Projected by CMIP6 Models With Observational Constraints Under a High GHG Emission Scenario

Fa Li[1,2], **Qing Zhu**[1] , **William J. Riley**[1] , **Kunxiaojia Yuan**[1,2], **Huayi Wu**[2], **and Zhipeng Gui**[2]

[1]Climate and Ecosystem Sciences Division, Climate Sciences Department, Lawrence Berkeley National Laboratory, Berkeley, CA, USA, [2]State Key Laboratory of Information Engineering in Surveying, Mapping and Remote Sensing, Wuhan University, Wuhan, China

Abstract As the world's fifth-largest economy entity, California (CA) is vulnerable to climate changes especially the magnitude of winter (wet season) precipitation that is closely linked to regional drought severity, vegetation growth, and wildfire activities. However, the fate of CA precipitation in the future remains highly uncertain, for example, the state-of-the-art Earth system models (ESMs) from the Coupled Model Intercomparison Project Phase 6 (CMIP6) projected −3% to +42% and −27% to +63% precipitation changes in northern and central-southern CA, respectively, under the high greenhouse gas (GHG) emission scenario (SSP585). In this work, we applied the Pareto optimality concept and used observed teleconnection patterns (causal relationships between ocean regions and CA precipitation) to mechanistically constrain CMIP6 projected CA precipitations. We estimated that precipitation will robustly increase by 0.4–1.3 mm d^{-1} (10–34%) over northern CA and increase by 0.1–0.5 mm d^{-1} (7–32%) over central-southern CA by the end of the 21st century compared with present-day. Up to 71% of ESM projection uncertainties were reduced mainly due to the strong and consistent causal relationship between North American west coast sea level pressure and CA precipitation in both observations and CMIP6 models. Our results suggest that teleconnection patterns are powerful mechanistic constraints that can help explain and reduce uncertainties in ESM projections.

Plain Language Summary California (CA) has surpassed the United Kingdom and achieved the world's fifth-largest economy since 2018. However, ongoing climate change poses unprecedented challenges for California's economic growth through declining water resources, intensifying regional drought, and exacerbating wildfire activities. Winter precipitation (CA wet season) will play an increasingly important role in combating the regional dryout. Therefore, it is critically important to understand the future fate of CA winter precipitation. This study relied on the state-of-the-art Earth system model projections and observed teleconnection patterns to estimate the future CA precipitation under a high emission scenario. We found that CA winter precipitation will robustly increase by up to ∼34% till the end of 21st century. The enhanced precipitation will provide necessary water resources and more importantly will provide natural solutions to the environmental disturbances (e.g., wildfire).

1. Introduction

California winter precipitation has many influences on local ecosystems, agriculture, wildfire, and water resources (Chang et al., 2015; Lund et al., 2018; Westerling et al., 2006), and imposes challenges to management across the state. CA's Mediterranean climate has the majority of its precipitation occurring in winter (Swain et al., 2018). With anomalously lower winter precipitation and higher temperatures, CA has experienced one of the most severe droughts on record during 2012–2016, caused billions of dollars in economic losses and millions of tree deaths (Lund et al., 2018). Meanwhile, variation in winter precipitation affects fuel availability and flammability, which are closely linked to wildfire severity in the following dry season (Littell et al., 2009, 2016). Future winter precipitation changes in CA associated with global warming and enhanced potential evapotranspiration will directly affect the state's economy and environment. However, robust projection of CA precipitation remains challenging, as evidenced by the large discrepancy among state-of-the-art climate models (Allen & Luptowitz, 2017; Choi et al., 2016; Langenbrunner & Neelin, 2017b; Simpson et al., 2016). Considerable uncertainties exist in model projections of CA 21st century precipitation in the Climate Model Intercomparison Project (CMIP) versions 3 and 5 (Neelin et al., 2013) and, as we show here (Figure 1), the recent Coupled Model Intercomparison

Writing – review & editing: Qing Zhu, William J. Riley, Huayi Wu, Zhipeng Gui

Project Phase 6 (CMIP6). This uncertainty is attributable to internal variability (Deser et al., 2012; Thompson et al., 2015) and differences in modeling the responses of CA rainfall to tropical-midlatitude-Arctic atmospheric circulation changes (Allen & Luptowitz, 2017; Choi et al., 2016; Cvijanovic et al., 2017; S.-Y. S. Wang et al., 2017).

California lies within a transition zone between mid-to-high-latitude regions that are expected to become wetter and subtropical regions expected to be drier by the end of the 21st century (Neelin et al., 2013). The latitudinal differences of precipitation changes arise from the "rich-get-richer" mechanism, that is, tropical and mid-to-high-latitude (subtropical) regions of climatological moisture convergence (divergence) will become wetter (drier; Choi et al., 2016; Neelin et al., 2013). Teleconnections from pacific decadal oscillation (PDO; Choi et al., 2016), Indian ocean (Zhou et al., 2020), western pacific (Linkin & Nigam, 2008), southern pacific (Mamalakis et al., 2018), and Atlantic (Park et al., 2019) regions modulate CA winter precipitation. Further, future poleward expansion of the Hadley Cell (Choi et al., 2016) and Arctic Amplification (AA; Cvijanovic et al., 2017) could reduce CA precipitation, while possible increased southerlies on the North America (NA) west coast (Simpson et al., 2016) and mean circulation changes related to El Niño teleconnections (Allen & Luptowitz, 2017), may enhance CA precipitation. These complex teleconnections between CA precipitation and remote oceanic regions provide useful constraints for model predictions, and pose the challenge of comprehensively analyzing the teleconnections in the context of reducing model uncertainties.

Previous studies have focused on a specific remote region or single teleconnection linked to CA precipitation through correlation analysis (Chang et al., 2015; Choi et al., 2016; Neelin et al., 2013), while the relative importance of controls from different regions have not been explored from a causality perspective. Correlation can be highly biased by confounding effects from autocorrelation, indirect controls, and common drivers, leading to spurious, noncausal, and interpretability-limited relationships (Kretschmer et al., 2016; Runge, Bathiany, et al., 2019). Climate model experiments through a controlled perturbation of the system or idealized simulations can provide physically interpretable causal links (Allen & Luptowitz, 2017; Cvijanovic et al., 2017; Simpson et al., 2016). However, opposing conclusions have been drawn (Allen & Luptowitz, 2017; Simpson et al., 2016) due to different choices of physical representations within the climate models. Constraining model performance to represent one specific causal link may tradeoff against the other causal links (Langenbrunner & Neelin, 2017b). The recently developed causal inference method (Runge, Bathiany, et al., 2019; Runge, Nowack, et al., 2019) provides a new way to evaluate interaction networks within climate model projections (Nowack et al., 2020), giving it the potential to assess the complex teleconnection networks affecting CA precipitation.

Here, we applied the causal discovery algorithm (Nowack et al., 2020; Runge et al., 2015) to observations (1979–2014) and 18 CMIP6 climate models (historical: 1979–2014, future: year 2020–2100, SSP585), to infer directional teleconnections that significantly modulate CA precipitation projections. The identified major teleconnections are then applied as constraints to reduce uncertainty in projected CA precipitation.

2. Data Sets and Methods

2.1. Data Sets and Preprocessing

Reanalysis and model simulated data sets of daily sea level pressure and precipitation are used in our studies. Reanalysis data sets include daily sea level pressure data from NCEP-NCAR, precipitation data set from Climate Prediction Center (CPC), and sea level pressure and precipitation data from European Centre for Medium-Range Weather Forecasts (ECMWF). Daily mean sea level pressure and precipitation data sets from 18 climate models in CMIP6 are used for historical (1979–2014) and future (2020–2100, the SSP585 emission scenario, O'Neill et al., 2016) analyses. For models with multiple runs, we first averaged multiple runs of each model, and used the calculated multirun average of each model for multimodel ensemble mean calculations and future climate change analysis (Chang et al., 2015; Neelin et al., 2013; Simpson et al., 2016). The model names, variable names, and their corresponding realization IDs are listed in Table S1 of Supporting Information S1. As we focus on intraseason atmospheric interactions at a weekly scale, each data set was aggregated to a weekly temporal resolution (Runge et al., 2015), and bi-linearly interpolated to $2.5° \times 2.5°$, which was the same spatial resolution to that of NCEP-NCAR data sets. To make time series stationary for causal inference, all data sets (including model simulated and reanalysis data sets of precipitation and sea level pressure) were detrended by removing the long-term (1979–2014) winter weekly mean and removing the linear trend in each anomaly data set (Nowack
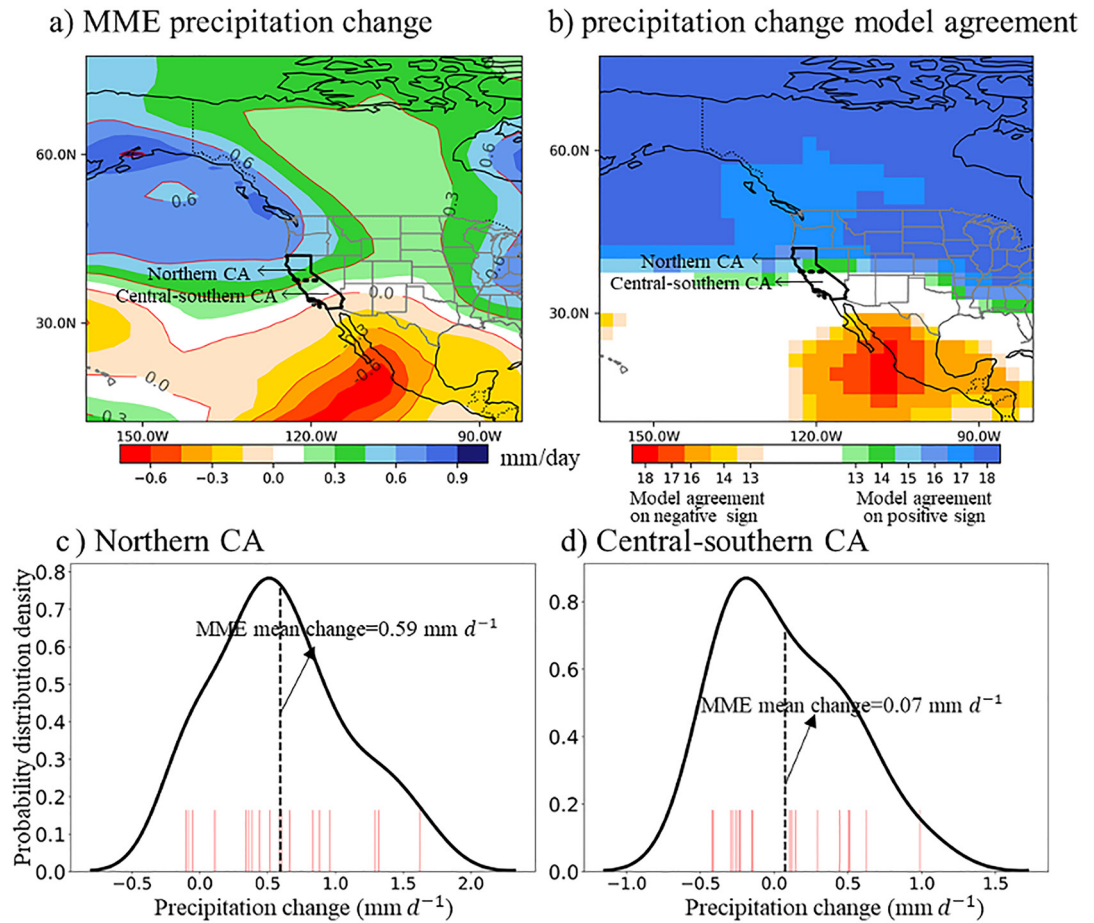
Figure 1. Unconstrained Climate Model Intercomparison Project (CMIP6) models project a wide range for future California precipitation. California (CA) winter (December, January, February) precipitation change of the multimodel ensemble means in CMIP6 for the end of century (2070–2100 average high emission scenario (SSP585)) relative to a historical period of 1979–2014. (a) Multimodel ensemble mean precipitation changes (mm d^{-1}). (b) Model agreement on the sign of precipitation changes among the model ensemble. Cold (warm) colors indicate the number of models (of 18) agreeing on positive (negative) precipitation change and passing a binomial test at a 95% confidence level, while white color represents nonsignificant ($p > 0.05$) changes. (c) Statistics of mean precipitation changes of CMIP6 models in northern California (38.8–42.4°N), and (d) central-southern California (32.0–38.8°N). Each red line in (c, d) represents precipitation change value of each individual climate model. The multimodel ensemble mean is computed by first averaging multiple available runs of each individual model, and the black dashed lines represent multimodel ensemble mean precipitation changes in northern and central-southern California.

et al., 2020; Runge et al., 2015). For precipitation data, considering future different change patterns in northern and central-southern CA (Figure 1), we calculated the areal average precipitation of each CA subregion, and used the areal average for subsequent evaluation and future precipitation change analysis.

2.2. Methods

A data driven causal discovery frame (Nowack et al., 2020; Runge et al., 2015) is used to infer the directed and time-lagged causal networks in observations and climate model simulations, and a multiobjective optimization method-Pareto optimality (Langenbrunner & Neelin, 2017a, 2017b) is used to choose an optimal subset of CMIP6 models for future precipitation change analysis based on inferred causal networks (the detailed workflow shown in Figure S1 of Supporting Information S1). In the causal discovery frame, varimax-rotated principal component analysis (PCA) was applied to global sea level pressure (SLP) anomaly data to extract components which can represent major modes of climate variability (Hannachi et al., 2007; Nowack et al., 2020; Runge et al., 2015; Vejmelka et al., 2015). PCMCI (PC is named after its inventors, Peter Spirtes and Clark Glymour

(Spirtes et al., 2000), and MCI is the acronym for momentary conditional independence; Runge, Nowack, et al., 2019), which is particularly suitable for high-dimensional and autocorrelated climate data, was used to exclude confounding effects and identify causal controls from different regions on CA rainfall.

Principal component analysis (PCA) followed by a Varimax rotation (PCA-Varimax) is a dimension reduction method to extract large-scale regional climatological processes (Hannachi et al., 2007; Nowack et al., 2020; Runge et al., 2015; Vejmelka et al., 2015). PCA, also referred as empirical orthogonal functions (EOFs), has been numerously used to identify global or regional components of climate variability, such as ENSO (Alexander et al., 2002), Pacific Decadal Oscillation (PDO; Newman et al., 2016), and North Pacific Oscillation (NPO; Linkin & Nigam, 2008; Yu & Kim, 2011). Traditional PCA without rotation shows limitations to spatially and explicitly split contributions from different physically defined climate processes with nonorthogonal time series, therefore making patterns more difficult to interpret (Guilloteau et al., 2021; Nowack et al., 2020). Varimax rotation on leading components of PCA makes the loading of weights at different grid locations either large or very small, allowing spatial patterns associated with the components to become more localized and reflect modes for actual physical processes (Nowack et al., 2020; Runge et al., 2015). Here, to remove noisy components, we used a truncated PCA. For sea level pressure (SLP) data, we obtained components through PCA that explained more than 95% of global SLP variance for further rotation. We then selected 26 components (Figure 2) that explained about 69% of SLP-related variance and had been shown to directly or indirectly affect CA precipitation in the literature (the references of related regions and their corresponding links to CA precipitation are listed in Table S2 of Supporting Information S1). We here estimated the components using 36-year observations (1979–2014), and used the estimated weights to consistently extract component time series of SLP during historical period (1979–2014) and future period (2020–2100) from CMIP6 (Nowack et al., 2020).

PCMCI is used to infer atmospheric interactions between different regions (Runge et al., 2015). Compared to commonly used Granger causality method, PCMCI significantly improves the detection power (true-positive rate) of causal links when the analyzed systems have high-dimensional variables and strong autocorrelation, both of which are relevant in our studies (Runge, Bathiany, et al., 2019; Runge, Nowack, et al., 2019). Two steps, PC (named after Peter Spirtes and Clark Glymour, Spirtes et al., 2000), and MCI (momentary conditional independence) test, are included in the PCMCI method. To test whether there exists a causal link from a driver to a target variable (e.g., the causal link from X to Y), the first step, PC, iteratively performs conditional independence tests and selects the typically few relevant necessary confounders (e.g., the confounder set Z). The second step, MCI, uses the necessary confounders (e.g., the confounder set Z) selected in the PC step, to further conduct a conditional independence test (e.g., test whether X and Y are conditionally independent given Z), alleviating the problem of strong autocorrelation and achieving final causal link inference. Compared with directly using all potential drivers as confounders, the PC step filters out necessary fewer confounders and feeds them into MCI for the conditional independence test, thereby avoiding conditioning on high-dimensional variables that lowers causal link detection power (Nowack et al., 2020; Runge et al., 2015). Details of the PCMCI method can be found in Runge, Nowack, et al. (2019). Generally, conditional independence test methods in PC and MCI can be linear or nonlinear. Here, we used a partial correlation method for conditional independence test, and the absolute value of partial correlation coefficient in the MCI step was used to measure the causal strength. We focused on linear causal links between different SLP regions and linear causal controls from different SLP regions on CA precipitation. The parameter, maximum time lag of PCMCI, was set to 4 weeks, as we focused on intra-seasonal atmospheric interactions at a weekly time resolution, and expected dependencies to be stationary (Runge et al., 2015). The time lags ranged from −4 to 0 weeks, where a negative time lag represented a time-lagged causal control and a time lag of 0 represented dependency within a week (Runge et al., 2015; Runge, Bathiany, et al., 2019). We selected candidate conditions with a significance level of α, which was optimized using the Akaike information criterion (among pc-α = 0.05, 0.1, 0.2; Nowack et al., 2020). The final links are statistically significant (two-tailed Student's t test, p value < 0.05). Since causal interactions between different seasons may differ (Nowack et al., 2020), and most of CA rainfall occurs in winter, we construct the causal network in December, January, February (DJF; Allen & Luptowitz, 2017; Neelin et al., 2013).

Similar to the causal network evaluation method in Nowack et al. (2020), we applied the widely used F_1-score to compare the causal network similarity between observations and models considering the imbalance of the number of true links and nonlinks (true links only account for about 6% of all possible links in the network).
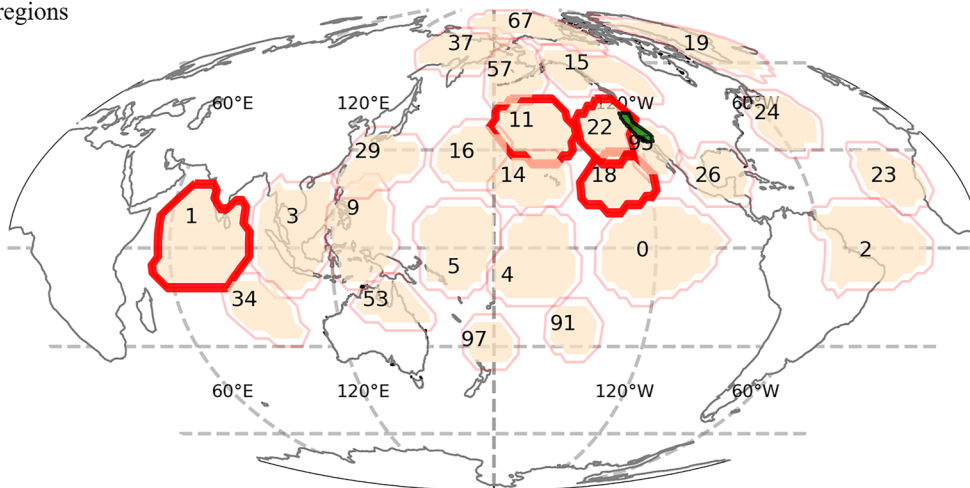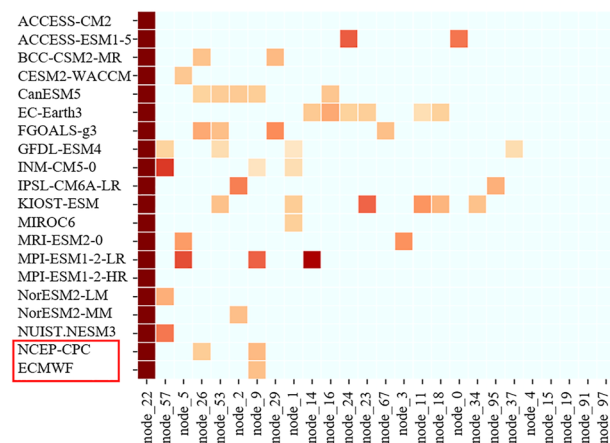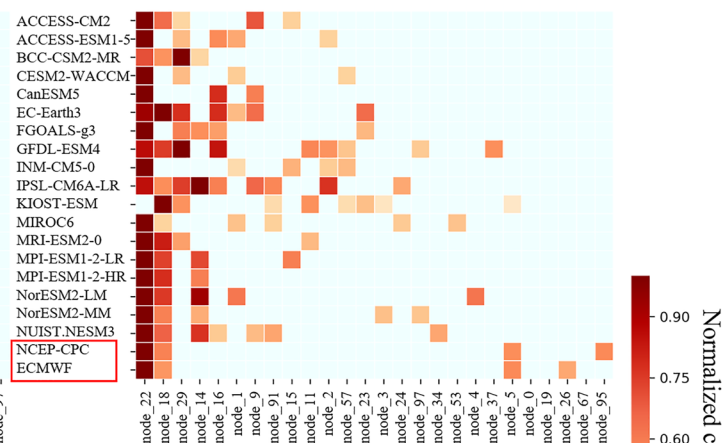
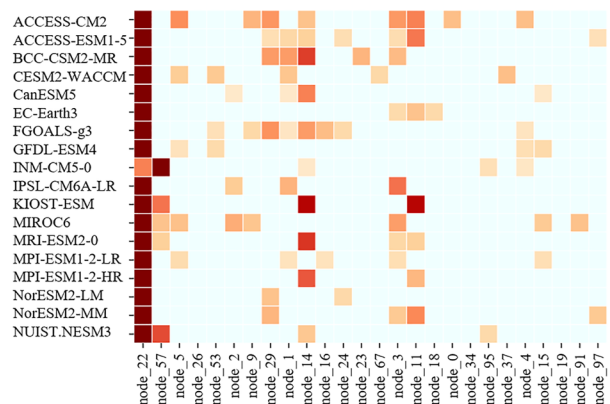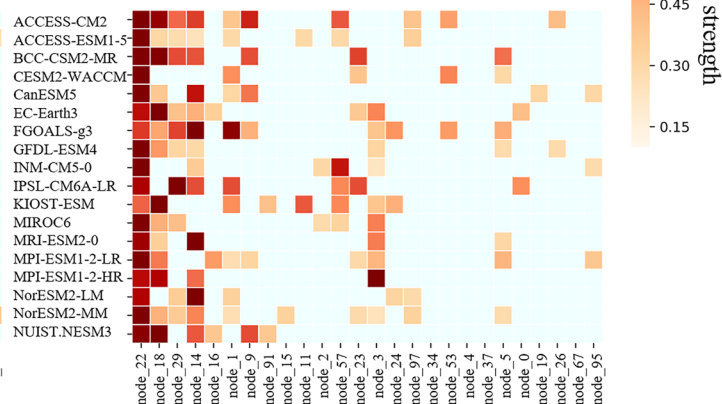**Figure 2.** Critical regions with sea level pressure (SLP) significantly affect California (CA) precipitation during historical and future periods. Critical regions that may directly or indirectly affect winter rainfall in CA (a), and time-lagged causal control strengths from SLP of different regions on CA precipitation (b) for northern CA precipitation during 1979–2014; (c) for central-southern CA precipitation during 1979–2014; (d) for northern CA precipitation during 2020–2100; (e) for central-southern CA precipitation during 2020–2100. In (a), the location of each region (node) is determined by its corresponding spatial loading calculated from Varimax-principal component analysis (PCA), and the number on each region represents the order of each component in all components (explain more than 95% variance of global sea level pressure) calculated by Varimax-PCA. In (b–e), the strength of causal control in each row was normalized to a 0–1 range using the row's maximum control strength, and unnormalized strength of causal control is shown in Figure S2 of Supporting Information S1. Stronger controls are shown with deeper red colors, and nonsignificant (p value > 0.05) controls are shown with the light-cyan color. Red boxes in (b, c) indicate observationally constrained reanalysis data sets.

F_1-score, based on the existence or nonexistence of links without consideration of link strength, balances precision and recall. It is defined by

$$F_1 = \frac{2 \times \text{Precision} \times \text{Recall}}{\text{Precision} + \text{Recall}} \tag{1}$$

$$\text{Precision} = \frac{\text{TP}}{\text{TP} + \text{FP}} \tag{2}$$

$$\text{Recall} = \frac{\text{TP}}{\text{TP} + \text{FN}} \tag{3}$$

where TP is the number of correct links exist in observations and models, and FP (FN) is the number of falsely detected links (not detected links) relative to observations. Considering that models may represent teleconnections reasonably well but with a bias in its time lag, a relaxation of time lag up to 1 week (if a causal link with the same sign of dependence to observation existed in models but its time lag differed from the observed one within 1 week, we treated the link as a corrected one) is applied when calculating each score (Nowack et al., 2020).

Pareto optimality is applied to identify an optimal subset of climate models that simultaneously achieve higher performance in terms of multiple observation-based evaluation metrics. Pareto optimality, named after Vilfredo Pareto (Ehrgott, 2012), is a multiobjective optimization technique that quantifies performance trade-offs across multiple metrics. The approach finds optimal models called the Pareto frontier that improve one measure of performance without degrading another (Branke et al., 2008; Langenbrunner & Neelin, 2017b; Shoval et al., 2012). In general, a single metric cannot capture multiple aspects of model performance. For example, traditional bias (e.g., root mean square error) or correlation-based metrics have been used for multimodel evaluation and intercomparison (Langenbrunner & Neelin, 2017b; Nowack et al., 2020; Sanderson et al., 2017); however, these metrics are not process-oriented and may lead to spurious relationships (Eyring et al., 2019; Runge, Bathiany, et al., 2019). By combining causal inference with Pareto optimality, we can constrain climate model ensemble projection uncertainties (the uncertainty is assessed using the range of projected changes, i.e., the maximum minus the minimum) in a more physically explainable way.

3. Results and Discussions

3.1. Uncertainty in CMIP6 Model Projected CA Precipitation Change and Dominant Drivers

Eighteen CMIP6 models (Table S1 in Supporting Information S1) were selected based on availability of daily historical and future precipitation (Pr) and sea level pressure (SLP) during historical and a high emission scenario (SSP585). A wide range of CA precipitation changes were predicted by the MultiModel Ensemble (MME; Figures 1a, 1c and 1d) and the large discrepancy in the signs of CMIP6 simulated CA precipitation changes (Figure 1b) was generally consistent with those of CMIP5 (Neelin et al., 2013), indicating the large uncertainties remained in CMIP6 models after a decade of model developments. Over northern CA, the CMIP6 MME mean precipitation increased by 0.59 mm d^{-1} (~15% of the observed historical mean during 1979–2014), and models agreed on the positive precipitation change (Figure 1b). The central-southern CA MME mean precipitation increased by 0.07 mm d^{-1} (~4% of the observed historical mean during 1979–2014). However, models did not agree on the signs of the change (failing a binomial test, p value > 0.05).

The observed causal networks revealed that both northern and central-southern CA precipitation were modulated by SLP at multiple remote oceanic regions, while the strongest controller was over the west coast of Northern America region (node 22, Figure 2, Table S2 in Supporting Information S1). These nodes are determined by spatial loading calculated from Varimax-PCA (see Section 2.2), and the number on each region represents the order of each component in all components (explaining more than 95% variance of global sea level pressure). References of all selected nodes are listed in Table S2 of Supporting Information S1. The majority of CMIP6 model causal networks also confirmed the strong teleconnection between node 22 SLP and CA precipitation (passing a binomial test at a 95% confidence level). Over node 22, the west coast higher pressure pushes storm tracks away from CA, resulting in anomalously drier winters (Choi et al., 2016; Cvijanovic et al., 2017; Seager et al., 2015, 2017), while lower pressure is robustly associated with wetter winters (Guirguis et al., 2020; Seager et al., 2015). Over the central-southern CA, both observation and the majority of CMIP6 models (13 out of 18)

a) Northern CA

b) Central-southern CA
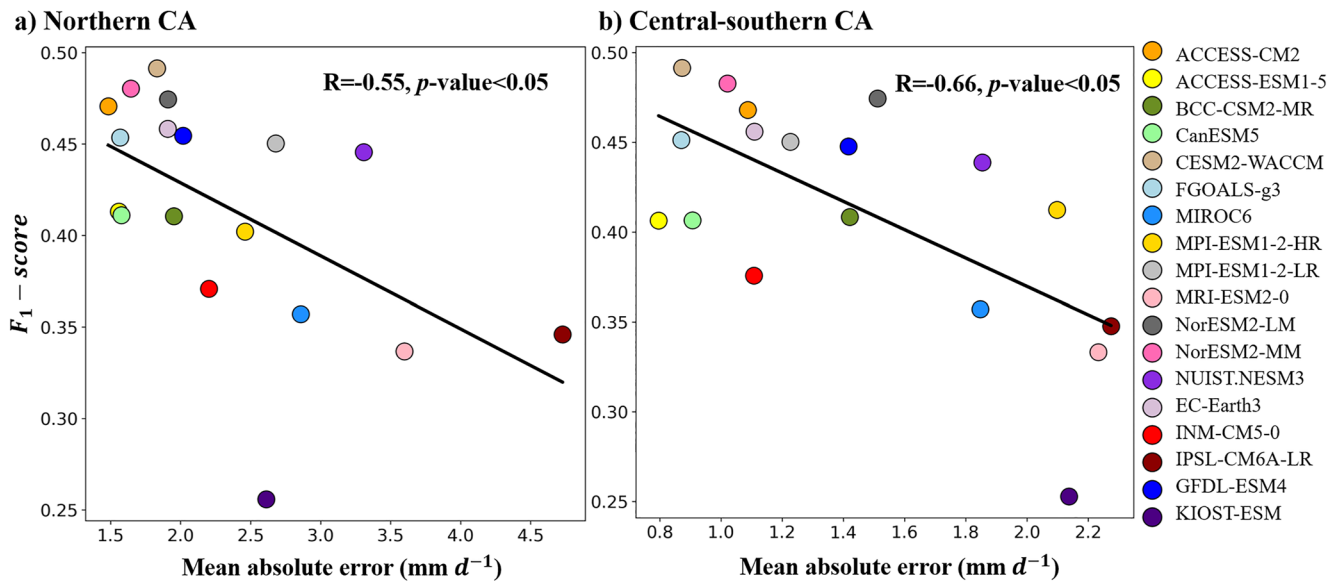
Figure 3. Relationship between model-data causal network similarity (F_1-score) and model bias for historical (1979–2014) California (CA) precipitation. (a) Northern CA and (b) central-southern CA. The F_1-score and model bias are evaluated relative to NCEP-NCAR SLP and Climate Prediction Center (CPC) precipitation reanalysis data sets (model evaluation results referring to European Centre for Medium-Range Weather Forecasts (ECMWF) data sets are shown in Figure S3 of Supporting Information S1). For precipitation bias, the areal average of each CA region (northern or central-southern region) is calculated first, then the mean absolute error between the observed and simulated areal average precipitation series is calculated. Here, the ensemble mean of precipitation bias is plotted.

agreed on the secondary control of northeastern pacific region (node 18) SLP on CA precipitation. The variations of SLP over node 18 were often associated with variations of SLP in tropical eastern pacific temperature and SLP, which were associated with El Niño events (Alexander et al., 2002; Yu & Kim, 2011).

In addition, our results confirmed that the controls from SLP over dominant remote oceanic regions (e.g., nodes 22, 18) on CA precipitation are conserved in future simulations, suggesting these teleconnections continue under future climate change (Figures 2b–2e). Several other independent analyses have also found sustainability of future teleconnections under global warming (Allen & Luptowitz, 2017) due to poleward expansion of the Hadley cell (Choi et al., 2016; Lu et al., 2007) or thermal expansion and robust west coast SLP trends (Swain et al., 2016).

3.2. Constraining CMIP6 Simulated CA Precipitation With Causal Networks

To quantify the agreement between observed and modeled causal networks, we compared the causal network similarity score (F_1-score metric, see Section 2.2) against the model bias during the historical period (1979–2014). Here, the causal link strength, which was also potentially important, was not considered when calculating the F_1-score because we focused on the causal network structure and considered the sparsity of the network structure (Nowack et al., 2020). This constraint helps identify an ensemble of models that more realistically represent atmospheric teleconnections important for CA precipitation. We found that CMIP6 models with higher F_1-scores (higher similarity to the observed networks) tended to have lower precipitation biases (mean absolute error) over both north (Pearson $r = -0.55$, $p < 0.05$, Figure 3a) and central-south CA (Pearson $r = -0.66$, $p < 0.05$, Figure 3b). These negative correlations were robust when using other bias evaluation metric (e.g., root mean square error) and adding two more models with daily historical simulations but without projections under the SSP585 scenario (Figure S3a in Supporting Information S1) or using alternative observationally constrained reanalysis data (Figure S3b in Supporting Information S1, ECMWF data sets). These results indicate that the SLP-CA precipitation causal relationship in CMIP6 models is an important constraint for simulated CA precipitation. Importantly for our next analysis, the CMIP6 dominant causal links were sustained in the future simulations (Figures 2d and 2e).

To evaluate robustness of future precipitation changes, MME-mean or weighted-MME methods are often used (Eyring et al., 2019). However, the prevailing one-model-one-vote MME mean method is often criticized because of diverse model skills and model interdependence (Abramowitz et al., 2019). Although weighted-MME
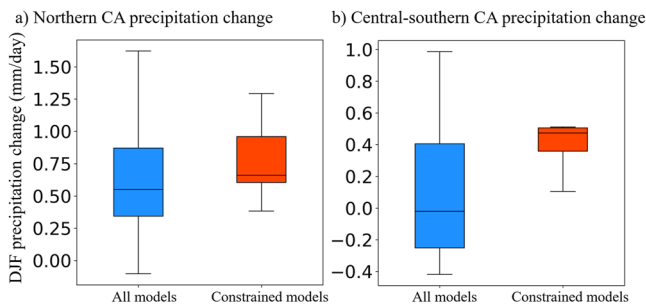
Figure 4. Causality-constrained Climate Model Intercomparison Project (CMIP6) models predict a wetter future California with lower uncertainty bounds. (a) Future precipitation changes (2070–2100 minus 1979–2014) over northern California (CA) and (b) central-southern CA. Boxes represent lower and upper quartiles (25th and 75th percentile) and the median (50th percentile), and whiskers span the range (minimum and maximum) of the full distributions.

methods consider model skills and independence (Knutti et al., 2017; Sanderson et al., 2017), how to assign weights to each model is not always clear (Langenbrunner & Neelin, 2017b; Stocker, 2014; B. Wang et al., 2018). Here, we used the multiobjective optimization concept-Pareto optimality (see Section 2.2) to choose a subset of CMIP6 models for future precipitation change analysis. The Pareto optimality has been widely used to balance metric trade-offs in different disciplines, including climate model parameterization (Langenbrunner & Neelin, 2017a) and precipitation analysis (Langenbrunner & Neelin, 2017b). The Pareto-optimal subsets of models with higher F_1-score, lower MAE in historical CA precipitation, and higher mutual information (a nonlinear correlation-based metric to measure the consistency) (Hlinka et al., 2014; Pechlivanidis et al., 2018) between simulated and observed node 22 SLP, were selected over northern and central-southern CA using an orthogonal array-based method (Eendebak & Vazquez, 2019; Schoen et al., 2010). The constrained optimal models (models marked out in Table S1 of Supporting Information S1) showed wetter future conditions in CA (Figure 4) with mean precipitation increased by 0.78 mm d^{-1} in northern CA (~20% compared to observed 1979–2014 mean), and increased by 0.39 mm d^{-1} in central-southern CA (~25% of observed 1979–2014 mean).

The findings of future increase in winter precipitation of CA are consistent with the results in (Allen & Anderson, 2018; Allen & Luptowitz, 2017; Langenbrunner & Neelin, 2017b; Zecca et al., 2018). Our results are robust even when included five additional suboptimal models (marked out in Table S1 of Supporting Information S1) that showed mean precipitation increased by 0.81 mm d^{-1} in northern CA and 0.35 mm d^{-1} in central-southern CA. Further, the uncertainty range for future CA precipitation changes was reduced by 47% (0.9 versus 1.7 mm d^{-1}) in northern CA and by 71% (0.4 versus 1.4 mm d^{-1}; Figure 4).

3.3. Tracing the Sources of Dominant Controls on CA Precipitation

In addition to the fact that SLP variation over the west coast of North American (node 22) strongly controlled both northern and central-southern CA precipitation (Figure 2), most of the CMIP6 models agreed with the observed nodes 18, 11, and 1 SLP controls on node 22 SLP variation (Figure 5a), and that these controls are sustained in the future (Figure 5b). Higher pressure (lower pressure) in north-central (node 11) and subtropical eastern pacific (node 18) was associated with higher (lower) SLP in node 22 (Figures 5c and 5d), while the signs of the relationship between SLP in the west Indian ocean (node 1) and node 22 were opposite (Figure 5e). Higher pressure in node 11 was suggested to be a factor for steering the wet winter air masses away from CA (Cvijanovic et al., 2017; Guirguis et al., 2020).

Lower pressure in node 18 was significantly associated with anomalously lower pressure and higher sea surface temperature in tropical central-eastern pacific (nodes 0 and 4; Figures S4 and S5 in Supporting Information S1), coinciding with El Niño events which were suggested to be a nonnegligible driver for wetter CA winters in historical and future projections (Allen & Anderson, 2018; Allen & Luptowitz, 2017; Zecca et al., 2018). In addition to north-central and subtropical eastern Pacific, a significant relationship also exists between the west Indian ocean and west coast of CA. Oscillations of SLP in the western Indian ocean (node 1) have a strong relationship with the Madden-Julian oscillation (MJO; Oliver & Thompson, 2011), which modulate blocking (Henderson et al., 2016), and atmospheric rivers (Mundhenk et al., 2018) in the northeast pacific, leading to profound regional impacts along the west coast of North America (Zhou et al., 2020). Our results revealed the robustness and consistency of these three distinct causal relationships associated with CA precipitation in both observations and CMIP6 models.

Future SLP changes over the dominant nodes explained why constrained models showed wetter precipitation changes in CA. Compared to MME projected mean SLP changes, the constrained optimal models consistently showed lower SLP conditions over node 22 (Figure 6a) with future mean SLP decreased by 1.27 hPa, which was robustly associated with wetter winters in CA (Seager et al., 2015; S.-Y. S. Wang et al., 2017). Compared to MME mean SLP changes, constrained optimal models showed lower SLP mean changes over node 18 (−0.44 versus 0.04 hPa, Figure 6b) and node 11 (−0.22 versus 0.75 hPa, Figure 6c), and higher SLP changes over node 1 (0.56
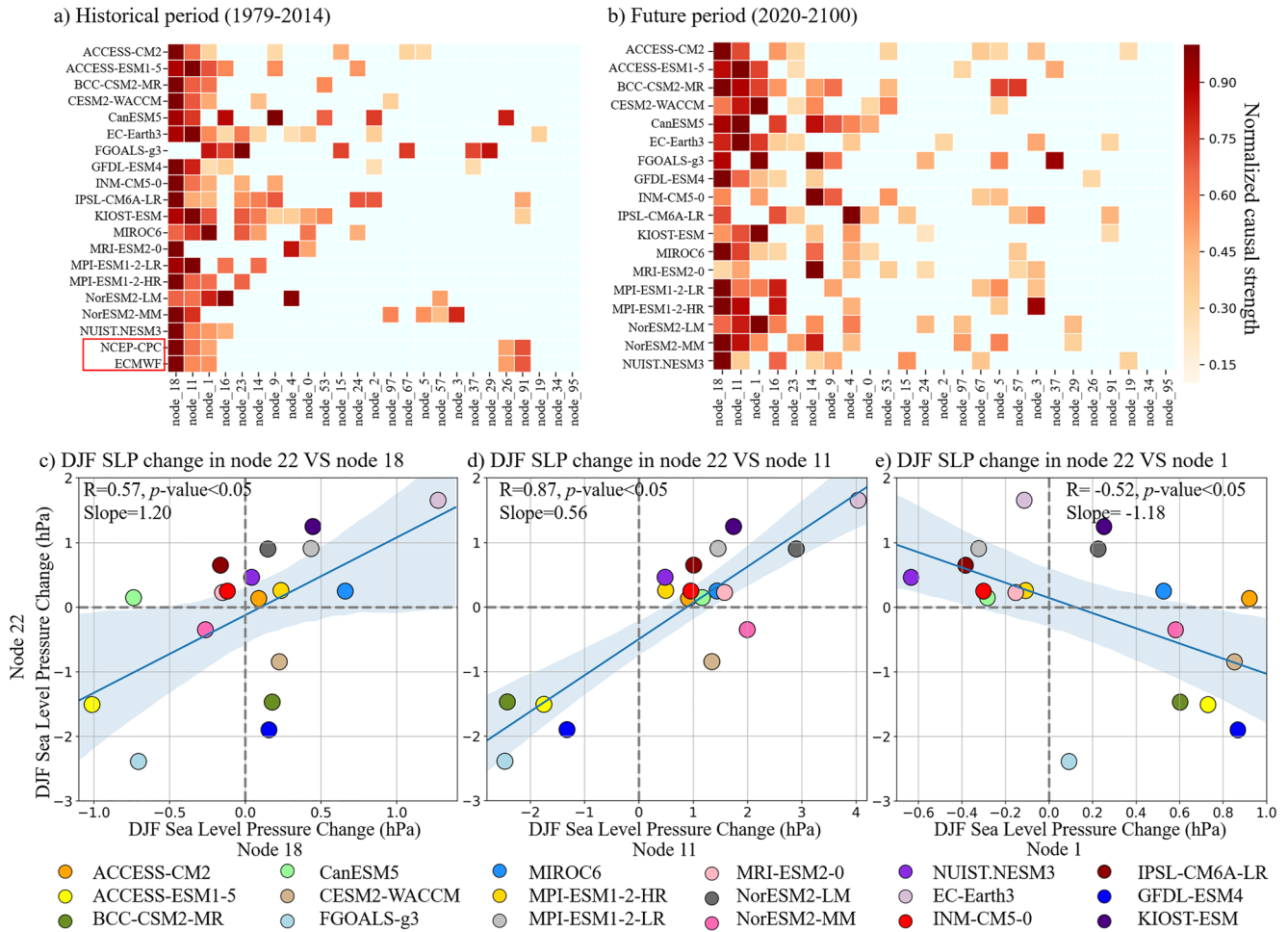
Figure 5. Time-lagged causal control strengths from sea level pressure (SLP) variation over remote oceanic regions on SLP variation over the west coast of North American (node 22): (a) 1979–2014. (b) 2020–2100. (c) Relationships between node 22 and node 18 SLP. (d) Relationships between node 22 and node 11 SLP. (e) Relationships between node 22 and node 1 SLP. Red boxes indicate observationally constrained reanalysis data in (a).

versus 0.19 hPa, Figure 6d). Further, the uncertainty range for future SLP changes was reduced by 50% (2.04 versus 4.04 hPa) in node 22%, 46% in node 18 (1.24 versus 2.29 hPa), 31% in node 11 (4.46 versus 6.51 hPa), and 51% in node 1 (0.76 versus 1.55 hPa; Figure 6). Compared to the SLP change ranges over node 22, 18, and 1, constrained optimal models over node 11 showed larger spread of SLP changes with lower SLP uncertainty reduction rate and different signs of SLP changes (Figure 6c), implying that uncertainty in node 11 needs to be further explored. As precipitation in CA was directly and negatively associated with SLP over node 22, decreased SLP in node 22 (Figure 6a) suggested increased precipitation in CA. SLP over node 22 was positively associated with SLP in nodes 18 (Figure 5c) and 11 (Figure 5d), and negatively associated with SLP in node 1 (Figure 5e). Therefore, lower SLP in nodes 18 and 11 along with higher SLP in node 1 consistently implied lower SLP in node 22. These results confirmed the inferred causal controls from nodes 22, 11, 18, node 1 on future wetter CA precipitation changes. We highlight the complexity of precipitation associated causal networks and the usefulness of using the causal networks to constrain projection uncertainties.

4. Conclusions

In summary, we identified the role that sea level pressure in critical oceanic regions has on California winter precipitation in observations and CMIP6 simulations. We showed that climate models with more realistic causal networks tend to have lower present-day precipitation biases in both northern and central-southern CA. Variability and future winter precipitation changes in CA are strongly controlled by SLP off the west coast
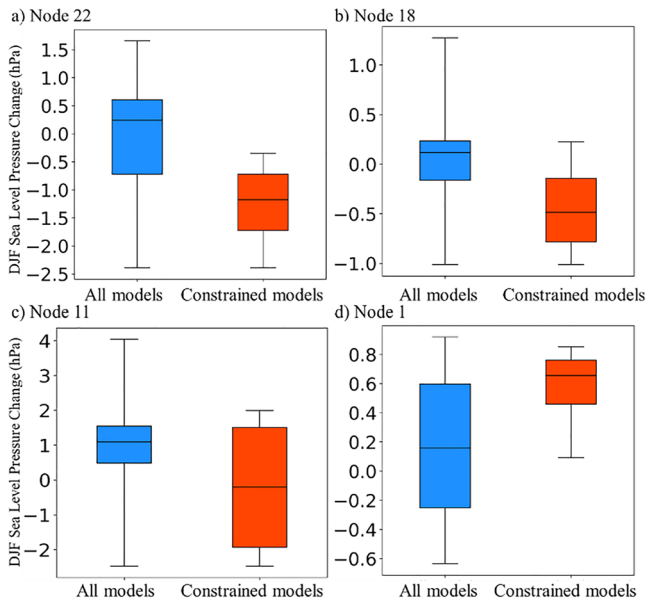
Figure 6. Comparison of all model and constrained model projected sea level pressure changes over critical regions. Future sea level pressure changes (2070–2100 minus 1979–2014) over nodes (a) 22, (b) 18, (c) 11, and (d) 1. Boxes represent lower and upper quartiles (25th and 75th percentile) and the median (50th percentile), and whiskers span the range (minimum and maximum) of the full distributions.

of Northern America. CMIP6 models constrained by observed causal structures, precipitation, and SLP over the identified dominant regions projected wetter end-of-century northern and central-southern California regions (mean precipitation increased by 20% and 25%, respectively), with much lower uncertainty ranges. CA drought in recent decades was suggested to be intensified compared to that in earlier history (Diffenbaugh et al., 2015; Williams et al., 2022), while our results showed increased precipitation at the end of 21st century compared to precipitation observations of recent decades. The reason for the difference may be attributed to future intensified teleconnections that could increase CA precipitation (Allen & Luptowitz, 2017; Cai et al., 2015; Zecca et al., 2018; Zhou et al., 2020). Our causal networks identified the dominant controllers of present and future CA precipitation to be SLP over the eastern pacific, north-central pacific, and west Indian ocean, relationships supported by previous studies (Allen & Luptowitz, 2017; Choi et al., 2016; Cvijanovic et al., 2017; Zhou et al., 2020). Our identified causal networks therefore provide powerful constraints for narrowing the spread of CMIP6 model projected precipitation in CA and should be applied to other regions and climate variables.

Data Availability Statement

All data sets and code are publicly available. Links of used data sets and code are listed below. NCEP-NCAR sea level pressure data: https://psl.noaa.gov/data/gridded/data.ncep.reanalysis.html; CPC precipitation data: https://psl.noaa.gov/data/gridded/data.cpc.globalprecip.html; ECMWF data: https://www.ecmwf.int/en/forecasts/datasets/-reanalysis-datasets/era-interim; COBE SST2 data set: https://psl.noaa.gov/data/gridded/data.cobe2.html. CMIP6 data: https://esgf-node.llnl.gov/search/cmip6. PCMCI code: https://github.com/jakobrunge/tigramite; PCA-Varimax code: https://github.com/peernow/CME_NCOMMS_2020. Pareto optimality code: https://oapackage.readthedocs.io/en/latest/examples/example_pareto.html.

References

Abramowitz, G., Herger, N., Gutmann, E., Hammerling, D., Knutti, R., Leduc, M., et al. (2019). ESD reviews: Model dependence in multi-model climate ensembles: Weighting, sub-selection and out-of-sample testing. *Earth System Dynamics*, *10*, 91–105. https://doi.org/10.5194/esd-10-91-2019

Alexander, M. A., Bladé, I., Newman, M., Lanzante, J. R., Lau, N.-C., & Scott, J. D. (2002). The atmospheric bridge: The influence of ENSO teleconnections on air-sea interaction over the global oceans. *Journal of Climate*, *15*, 2205–2231. https://doi.org/10.1175/1520-0442(2002)015<2205:TABTIO>2.0.CO;2

Allen, R. J., & Anderson, R. G. (2018). 21st century California drought risk linked to model fidelity of the El Niño teleconnection. *npj Climate and Atmospheric Science*, *1*, 1–14. https://doi.org/10.1038/s41612-018-0032-x

Allen, R. J., & Luptowitz, R. J. (2017). El Niño-like teleconnection increases California precipitation in response to warming. *Nature Communications*, *8*, 1–15. https://doi.org/10.1038/ncomms16055

Branke, J., Branke, J., Deb, K., Miettinen, K., & Słowiński, R. (Eds.). (2008). *Multiobjective optimization: Interactive and evolutionary approaches* (Vol. 5252). Springer Science & Business Media.

Cai, W., Santoso, A., Wang, G., Yeh, S.-W., An, S.-I., Cobb, K. M., et al. (2015). ENSO and greenhouse warming. *Nature Climate Change*, *5*, 849–859. https://doi.org/10.1038/nclimate2743

Chang, E. K., Zheng, C., Lanigan, P., Yau, A. M., & Neelin, J. D. (2015). Significant modulation of variability and projected change in California winter precipitation by extratropical cyclone activity. *Geophysical Research Letters*, *42*, 5983–5991. https://doi.org/10.1002/2015GL064424

Choi, J., Lu, J., Son, S. W., Frierson, D. M., & Yoon, J. H. (2016). Uncertainty in future projections of the North Pacific subtropical high and its implication for California winter precipitation change. *Journal of Geophysical Research: Atmospheres*, *121*, 795–806. https://doi.org/10.1002/2015JD023858

Cvijanovic, I., Santer, B. D., Bonfils, C., Lucas, D. D., Chiang, J. C., & Zimmerman, S. (2017). Future loss of Arctic sea-ice cover could drive a substantial decrease in California's rainfall. *Nature Communications*, *8*, 1–10. https://doi.org/10.1038/s41467-017-01907-4

Deser, C., Knutti, R., Solomon, S., & Phillips, A. S. (2012). Communication of the role of natural variability in future North American climate. *Nature Climate Change*, *2*, 775–779. https://doi.org/10.1038/nclimate1562

Diffenbaugh, N. S., Swain, D. L., & Touma, D. (2015). Anthropogenic warming has increased drought risk in California. *Proceedings of the National Academy of Sciences of the United States of America*, *112*, 3931–3936. https://doi.org/10.1073/pnas.1422385112

Eendebak, P. T., & Vazquez, A. R. (2019). OApackage: A Python package for generation and analysis of orthogonal arrays, optimal designs and conference designs. *Journal of Open Source Software*, *4*, 1097. https://doi.org/10.21105/joss.01097

Ehrgott, M. (2012). Vilfredo Pareto and multi-objective optimization. *Doc. Math* (pp. 447–453).

Eyring, V., Cox, P. M., Flato, G. M., Gleckler, P. J., Abramowitz, G., Caldwell, P., et al. (2019). Taking climate model evaluation to the next level. *Nature Climate Change*, *9*, 102–110. https://doi.org/10.1038/s41558-018-0355-y

Guilloteau, C., Mamalakis, A., Vulis, L., Le Phong, V. V., Georgiou, T. T., & Foufoula-Georgiou, E. (2021). Rotated spectral principal component analysis (rsPCA) for identifying dynamical modes of variability in climate systems. *Journal of Climate*, *34*, 715–736. https://doi.org/10.1175/JCLI-D-20-0266.1

Guirguis, K., Gershunov, A., Deflorio, M. J., Shulgina, T., Delle Monache, L., Subramanian, A. C., et al. (2020). Four atmospheric circulation regimes over the North Pacific and their relationship to California precipitation on daily to seasonal timescales. *Geophysical Research Letters*, *47*, e2020GL087609. https://doi.org/10.1029/2020GL087609

Hannachi, A., Jolliffe, I., & Stephenson, D. B. (2007). Empirical orthogonal functions and related techniques in atmospheric science: A review. *International Journal of Climatology: A Journal of the Royal Meteorological Society*, *27*, 1119–1152. https://doi.org/10.1002/joc.1499

Henderson, S. A., Maloney, E. D., & Barnes, E. A. (2016). The influence of the Madden-Julian oscillation on Northern Hemisphere winter blocking. *Journal of Climate*, *29*, 4597–4616. https://doi.org/10.1175/JCLI-D-15-0502.1

Hlinka, J., Hartman, D., Vejmelka, M., Novotná, D., & Paluš, M. (2014). Non-linear dependence and teleconnections in climate data: Sources, relevance, nonstationarity. *Climate Dynamics*, *42*, 1873–1886. https://doi.org/10.1007/s00382-013-1780-2

Knutti, R., Sedláček, J., Sanderson, B. M., Lorenz, R., Fischer, E. M., & Eyring, V. (2017). A climate model projection weighting scheme accounting for performance and interdependence. *Geophysical Research Letters*, *44*, 1909–1918. https://doi.org/10.1002/2016GL072012

Kretschmer, M., Coumou, D., Donges, J. F., & Runge, J. (2016). Using causal effect networks to analyze different Arctic drivers of midlatitude winter circulation. *Journal of Climate*, *29*, 4069–4081. https://doi.org/10.1175/JCLI-D-15-0654.1

Langenbrunner, B., & Neelin, J. (2017a). Multiobjective constraints for climate model parameter choices: Pragmatic Pareto fronts in CESM1. *Journal of Advances in Modeling Earth Systems*, *9*, 2008–2026. https://doi.org/10.1002/2017MS000942

Langenbrunner, B., & Neelin, J. D. (2017b). Pareto-optimal estimates of California precipitation change. *Geophysical Research Letters*, *44*, 12436–12446. https://doi.org/10.1002/2017GL075226

Linkin, M. E., & Nigam, S. (2008). The North Pacific Oscillation–west Pacific teleconnection pattern: Mature-phase structure and winter impacts. *Journal of Climate*, *21*, 1979–1997. https://doi.org/10.1175/2007JCLI2048.1

Littell, J. S., Mckenzie, D., Peterson, D. L., & Westerling, A. L. (2009). Climate and wildfire area burned in Western US ecoprovinces, 1916–2003. *Ecological Applications*, *19*, 1003–1021. https://doi.org/10.1890/07-1183.1

Littell, J. S., Peterson, D. L., Riley, K. L., Liu, Y., & Luce, C. H. (2016). A review of the relationships between drought and forest fire in the United States. *Global Change Biology*, *22*, 2353–2369. https://doi.org/10.1111/gcb.13275

Lu, J., Vecchi, G. A., & Reichler, T. (2007). Expansion of the Hadley cell under global warming. *Geophysical Research Letters*, *34*, L06805. https://doi.org/10.1029/2006GL028443

Lund, J., Medellin-Azuara, J., Durand, J., & Stone, K. (2018). Lessons from California's 2012–2016 drought. *Journal of Water Resources Planning and Management*, *144*, 04018067. https://doi.org/10.1061/(asce)wr.1943-5452.0000984

Mamalakis, A., Yu, J.-Y., Randerson, J. T., Aghakouchak, A., & Foufoula-Georgiou, E. (2018). A new interhemispheric teleconnection increases predictability of winter precipitation in southwestern US. *Nature Communications*, *9*, 1–10. https://doi.org/10.1038/s41467-018-04722-7

Mundhenk, B. D., Barnes, E. A., Maloney, E. D., Baggett, C. F., & Science, A. (2018). Skillful empirical subseasonal prediction of landfalling atmospheric river activity using the Madden-Julian oscillation and quasi-biennial oscillation. *npj Climate and Atmospheric Science*, *1*, 1–7. https://doi.org/10.1038/s41612-017-0008-2

Neelin, J. D., Langenbrunner, B., Meyerson, J. E., Hall, A., & Berg, N. (2013). California winter precipitation change under global warming in the Coupled Model Intercomparison Project phase 5 ensemble. *Journal of Climate*, *26*, 6238–6256. https://doi.org/10.1175/JCLI-D-12-00514.1

Newman, M., Alexander, M. A., Ault, T. R., Cobb, K. M., Deser, C., Di Lorenzo, E., et al. (2016). The Pacific decadal oscillation, revisited. *Journal of Climate*, *29*, 4399–4427. https://doi.org/10.1175/JCLI-D-15-0508.1

Nowack, P., Runge, J., Eyring, V., & Haigh, J. D. (2020). Causal networks for climate model evaluation and constrained projections. *Nature Communications*, *11*, 1–11. https://doi.org/10.1038/s41467-020-15195-y

Oliver, E. C., & Thompson, K. R. (2011). A reconstruction of Madden-Julian oscillation variability from 1905 to 2008. *Journal of Climate*, *25*, 1996–2019. https://doi.org/10.1175/JCLI-D-11-00154.1

O'Neill, B. C., Tebaldi, C., Vuuren, D. P. V., Eyring, V., Friedlingstein, P., Hurtt, G., et al. (2016). *The Scenario Model Intercomparison Project (ScenarioMIP) for CMIP6* (Vol. 9, pp. 3461–3482). Geoscientific Model Development. https://doi.org/10.5194/gmd-9-3461-2016

Park, J.-H., Li, T., Yeh, S.-W., & Kim, H. J. (2019). Effect of recent Atlantic warming in strengthening Atlantic–Pacific teleconnection on interannual timescale via enhanced connection with the Pacific meridional mode. *Climate Dynamics*, *53*, 371–387. https://doi.org/10.1007/s00382-018-4591-7

Pechlivanidis, I., Gupta, H., & Bosshard, T. (2018). An information theory approach to identifying a representative subset of hydro-climatic simulations for impact modeling studies. *Water Resources Research*, *54*, 5422–5435. https://doi.org/10.1029/2017WR022035

Runge, J., Bathiany, S., Bollt, E., Camps-Valls, G., Coumou, D., Deyle, E., et al. (2019). Inferring causation from time series in Earth system sciences. *Nature Communications*, *10*, 1–13. https://doi.org/10.1038/s41467-019-10105-3

Runge, J., Nowack, P., Kretschmer, M., Flaxman, S., & Sejdinovic, D. J. (2019). Detecting and quantifying causal associations in large nonlinear time series datasets. *Science Advances*, *5*, eaau4996. https://doi.org/10.1126/sciadv.aau4996

Runge, J., Petoukhov, V., Donges, J. F., Hlinka, J., Jajcay, N., Vejmelka, M., et al. (2015). Identifying causal gateways and mediators in complex spatio-temporal systems. *Nature Communications*, *6*, 1–10. https://doi.org/10.1038/ncomms9502

Sanderson, B. M., Wehner, M., & Knutti, R. (2017). Skill and independence weighting for multi-model assessments. *Geoscientific Model Development*, *10*, 2379–2395. https://doi.org/10.5194/gmd-10-2379-2017

Schoen, E. D., Eendebak, P. T., & Nguyen, M. V. (2010). Complete enumeration of pure-level and mixed-level orthogonal arrays. *Journal of Combinatorial Designs*, *18*, 123–140. https://doi.org/10.1002/jcd.20270

Seager, R., Henderson, N., Cane, M. A., Liu, H., & Nakamura, J. (2017). Is there a role for human-induced climate change in the precipitation decline that drove the California drought? *Journal of Climate*, *30*, 10237–10258. https://doi.org/10.1175/JCLI-D-17-0192.1

Seager, R., Hoerling, M., Schubert, S., Wang, H., Lyon, B., Kumar, A., et al. (2015). Causes of the 2011–14 California drought. *Journal of Climate*, *28*, 6997–7024. https://doi.org/10.1175/JCLI-D-14-00860.1

Shoval, O., Sheftel, H., Shinar, G., Hart, Y., Ramote, O., Mayo, A., et al. (2012). Evolutionary trade-offs, Pareto optimality, and the geometry of phenotype space. *Science*, *336*(6085), 1157–1160. https://doi.org/10.1126/science.1217405

Simpson, I. R., Seager, R., Ting, M., & Shaw, T. A. (2016). Causes of change in Northern Hemisphere winter meridional winds and regional hydroclimate. *Nature Climate Change*, *6*, 65–70. https://doi.org/10.1038/nclimate2783

Spirtes, P., Glymour, C. N., Scheines, R., & Heckerman, D. (2000). *Causation, prediction, and search*. MIT Press.

Stocker, T. (2014). *Climate change 2013: The physical science basis: Working Group I contribution to the fifth assessment report of the Intergovernmental Panel on Climate Change*. Cambridge University Press.

Swain, D. L., Horton, D. E., Singh, D., & Diffenbaugh, N. S. (2016). Trends in atmospheric patterns conducive to seasonal precipitation and temperature extremes in California. *Science Advances*, *2*, e1501344. https://doi.org/10.1126/sciadv.1501344

Swain, D. L., Langenbrunner, B., Neelin, J. D., & Hall, A. (2018). Increasing precipitation volatility in twenty-first-century California. *Nature Climate Change*, *8*, 427–433. https://doi.org/10.1038/s41558-018-0140-y

Thompson, D. W., Barnes, E. A., Deser, C., Foust, W. E., & Phillips, A. S. (2015). Quantifying the role of internal climate variability in future climate trends. *Journal of Climate*, *28*, 6443–6456. https://doi.org/10.1175/JCLI-D-14-00830.1

Vejmelka, M., Pokorná, L., Hlinka, J., Hartman, D., Jajcay, N., & Paluš, M. (2015). Non-random correlation structures and dimensionality reduction in multivariate climate data. *Climate Dynamics*, *44*, 2663–2682. https://doi.org/10.1007/s00382-014-2244-z

Wang, B., Zheng, L., Liu, D. L., Ji, F., Clark, A., & Yu, Q. (2018). Using multi-model ensembles of CMIP5 global climate models to reproduce observed monthly rainfall and temperature with machine learning methods in Australia. *International Journal of Climatology*, *38*, 4891–4902. https://doi.org/10.1002/joc.5705

Wang, S.-Y. S., Yoon, J.-H., Becker, E., & Gillies, R. (2017). California from drought to deluge. *Nature Climate Change*, *7*, 465–468. https://doi.org/10.1038/nclimate3330

Westerling, A. L., Hidalgo, H. G., Cayan, D. R., & Swetnam, T. W. (2006). Warming and earlier spring increase Western US forest wildfire activity. *Science*, *313*, 940–943. https://doi.org/10.1126/science.1128834

Williams, A. P., Cook, B. I., & Smerdon, J. E. (2022). Rapid intensification of the emerging southwestern North American megadrought in 2020–2021. *Nature Climate Change*, *12*(3), 1–3.

Yu, J.-Y., & Kim, S. T. (2011). Relationships between extratropical sea level pressure variations and the central Pacific and eastern Pacific types of ENSO. *Journal of Climate*, *24*, 708–720. https://doi.org/10.1175/2010JCLI3688.1

Zecca, K., Allen, R. J., & Anderson, R. G. (2018). Importance of the El Nino teleconnection to the 21st century California wintertime extreme precipitation increase. *Geophysical Research Letters*, *45*, 10648–10655. https://doi.org/10.1029/2018GL079714

Zhou, W., Yang, D., Xie, S.-P., & Ma, J. (2020). Amplified Madden-Julian oscillation impacts in the Pacific–North America region. *Nature Climate Change*, *10*, 654–660. https://doi.org/10.1038/s41558-020-0814-0